



Terrestrial exospheric dayside H-density profile at 3-15 R_e from UVIS/HDAC and TWINS Lyman- α data combined

Jochen H. Zoenchen¹, Hyunju K. Connor², Jaewoong Jung², Uwe Nass¹, and Hans J. Fahr¹

¹Argelander Institut für Astronomie, Astrophysics Department, University of Bonn, Auf dem Huegel 71, 53121 Bonn, Germany

²Geophysical Institute, University of Alaska Fairbanks, Alaska, USA

Correspondence to: J. H. Zoenchen (zoenn@astro.uni-bonn.de)

1 Abstract.

2 Terrestrial ecliptic dayside observations of the exospheric Lyman- α column intensity between 3-
3 15 Earth radii (R_e) by UVIS/HDAC at CASSINI have been analysed to derive the neutral exospheric
4 H-density profile at the Earth's ecliptic dayside in this radial range. The data were measured during
5 CASSINI's swing by manoeuvre at the Earth on 18 August 1999 and are published by (Werner
6 et al., 2004). In this study the dayside HDAC Lyman- α observations published by (Werner et al.,
7 2004) are compared to calculated Lyman- α intensities based on the 3D H-density model derived
8 from TWINS Lyman- α observations between 2008-2010 (Zoenchen et al., 2015). It was found, that
9 both Lyman- α profiles show a very similar radial dependence in particular between 3-8 R_e . Between
10 3.0-5.5 R_e impact distance Lyman- α observations of both TWINS and UVIS/HDAC are existing at
11 the ecliptic dayside. In this overlapping region the cross-calibration of the HDAC profile against
12 the calculated TWINS profile was done, assuming, that the exosphere there was similar for both
13 due to comparable space weather conditions. As result of the cross-calibration the conversion factor
14 between counts/s and Rayleigh $f_c=3.285$ [counts/s/R] is determined for these HDAC observations.
15 Using this factor the radial H-density profile for the Earths ecliptic dayside was derived from the
16 UVIS/HDAC observations, which constrained the neutral H-density there at 10 R_e to a value of 35
17 cm^{-3} . Furthermore, a faster radial H-density decrease was found at distances above 8 R_e ($\approx r^{-3}$)
18 compared to the lower distances 3-7 R_e ($\approx r^{-2.37}$). This increased loss of neutral H above 8 R_e
19 might indicate a higher rate of H ionization in the vicinity of the magnetopause at 9-11 R_e (near sub
20 solar point) and beyond, because of increasing charge exchange interactions of exospheric H atoms
21 with solar wind ions outside the magnetosphere.



22 **Keywords.** Atmospheric composition and structure (airglow and aurora; pressure, density, and tem-
23 perature) – meteorology and atmospheric dynamics (thermospheric dynamics)

24 1 Introduction

25 The Earth's exosphere is the outermost layer of our atmosphere that ranges from ≈ 500 km altitude
26 to beyond the Moon's orbit (Baliukin et al. 2019). Atomic hydrogen atom (H) becomes a dominant
27 species above an altitude of ≈ 1500 km. The exosphere gains and loses hydrogen atoms as a result of
28 the Sun - solar wind - magnetosphere - upper atmosphere interaction. Study of the exospheric density
29 distribution and its response to dynamic space environments is key to understand the past, present,
30 and future of the Earth's atmosphere and to infer the evolution of other planetary atmospheres.

31 The typical geocorona emission, i.e., solar Lyman- α photons resonantly scattered by hydrogen
32 atoms, has been a widely used dataset to derive a terrestrial exospheric neutral H-density. Sev-
33 eral spacecraft missions like Thermosphere - Ionosphere - Mesosphere Energetics and Dynamics
34 (TIMED; Kusnierkiewicz, 1997), Two Wide-Angle Imaging Neutral-Atom Spectrometer (TWINS;
35 Goldstein & McComas, 2018), and Solar and Heliospheric Observatory (SOHO; Domingo et al.,
36 1995) have observed the geocorona from various vantage points, covering an optically thick, near-
37 Earth exosphere below $\approx 3 R_e$ geocentric distance (e.g., Qin & Waldrop, 2016; Qin et al., 2017; Wal-
38 drop et al., 2013) to an optically thin, far distant exosphere on top (e.g., Bailey & Gruntman, 2011;
39 Cucho-Padin & Waldrop, 2019; Zoennchen et al., 2011, 2013). The exospheric density changes over
40 various time scales such as solar cycle (Waldrop & Paxton, 2013; Zoennchen et al., 2015; Baliukin
41 et al., 2019), solar rotation (Zoennchen et al., 2015), and geomagnetic storms (Bailey & Gruntman,
42 2013; Cucho-Padin & Waldrop, 2019; Qin et al., 2017; Zoennchen et al., 2017). This implies active
43 response of our exosphere to a dynamic space environment through physical processes like thermal
44 expansion, photoionization, and neutral charge exchanges as suggested in the previous theoretical
45 studies (Chamberlain, 1963; Bishop, 1985; Hodges, 1994; and references therein). Also the possible
46 contribution of non-thermal hydrogen to the exosphere is discussed (e.g., Qin & Waldrop, 2016;
47 Fahr et al., 2018).

48 Recently, exospheric neutral H-density at $10 R_e$ subsolar location becomes a particular interest
49 due to two upcoming missions, the NASA Lunar Environment heliospheric X-ray Imager (LEXI;
50 <http://sites.bu.edu/lexi>) and the joint ESA-China mission, Solar wind - Magnetosphere - Ionosphere
51 Link Explorer (SMILE; Branduardi-Raymont et al., 2018) with expected launches in 2023 and 2024,
52 respectively. Soft X-ray imagers on these spacecrafts will observe motion of the Earth's magne-
53 tosheath and cusps in soft X-ray with a primary goal of understanding the magnetopause reconnec-
54 tion modes under various solar wind conditions. Soft X-ray is emitted due to interaction between the
55 exospheric neutrals and the highly charged solar wind ions like O^{7+} and O^{8+} (Sibeck et al., 2018;
56 Connor et al., 2021). Neutral density is a key parameter that controls the strength of soft X-ray sig-



57 nals. Denser hydrogen increase their interaction probability with solar wind ions and thus enhance
58 soft X-ray signals, which is preferable for the LEXI and SMILE missions.

59 The dayside geocoronal observations above $8 R_e$ radial distance are very rare. For estimating an
60 exospheric density at $10 R_e$ subsolar location, Connor & Carter (2019) and Fuselier et al. (2010;
61 2020) used alternative datasets: the soft X-ray observations from the X-ray Multi-Mirror Mission-
62 Newton astrophysics mission (XMM; Jansen et al., 2001) and the Energetic Neutral Atom (ENA)
63 observations from the Interstellar Boundary Explorer (IBEX; McComas et al., 2009), respectively.
64 Their density estimates at $10 R_e$ show a large discrepancy, ranging from 4 cm^{-3} to 59 cm^{-3} with a
65 lower limit from the IBEX observations and an upper limit from the XMM observations. However,
66 these studies analyzed only a handful of events. Additionally, inherent difference of the soft X-ray
67 and ENA datasets leads to different density extraction techniques, possibly contributing to the neu-
68 tral density discrepancy. To understand a true nature of this outer dayside exosphere, more statistical
69 and cumulative approaches with various datasets are needed.

70 We estimate a dayside exospheric density in a radial distance of $3\text{-}15 R_e$ using rare dayside geo-
71 corona observations obtained from the CASSINI UVIS/HDAC Lyman- α instrument on 18 August
72 1999. This paper is structured as follows. Section 2 introduces the CASSINI Lyman- α observations
73 on 18 August 1999. Section 3 discusses the solar condition and interplanetary Lyman- α background
74 during the observation period. Section 4 explains our density extraction approach. Section 5 esti-
75 mates the conversion factor of the CASSINI UVIS/HDAC geocorona count rates to Rayleigh, and
76 Section 6 derives the dayside exospheric density profiles from the converted geocoronal emission in
77 Rayleigh. Finally, Section 7 discusses and concludes our results.

78

79 2 The UVIS/HDAC Lyman- α observations during CASSINI's swing by at the Earth

80 On its way to Saturn the CASSINI spacecraft performed a swing by manoeuvre at the Earth on 18
81 August 1999. The UVIS/HDAC Lyman- α instrument (FOV $\approx 3^\circ$) was switched on before and mea-
82 sured then continuously Lyman- α intensities during the manoeuvre. When approaching the Earth the
83 measured Lyman- α intensities were increasingly dominated by scattered Lyman- α emission from
84 neutral H-atoms of the terrestrial exosphere. The intensity profile in [counts/s] (averaged over a
85 1 min interval) from UVIS/HDAC is a rare observation of the exospheric dayside Lyman- α emis-
86 sion near the Earth-Sun line up to $15 R_e$ geocentric distance. It is a nearly perfect scan within the
87 ecliptic plane during ≈ 1.5 hours and therefore nearly free from latitudinal and temporal variations.
88 The profile was published by (Werner et al., 2004) and is shown in Figure 2 of their paper. From
89 each measurement they had subtracted 4500 [counts/s] as correction for their estimate of the inter-
90 planetary background intensity. For the geocentric distances $3\text{-}15 R_e$ this corrected profile can be



91 numerically approximated by the following fit function:

$$92 \quad I_{corr}(r) = 282920.2 * (r + 2.0)^{-2.2} \quad [counts/s] \quad (1)$$

93 with the geocentric distance r in R_e . In Figure 1 is shown, that the fitted radial intensity function
94 from Equation (1) (red line) approximates the profile from (Werner et al., 2004) (black line) very
95 well. Values from Equation (1) need to be re-added with 4500 [counts/s] in order to retrieve the
96 uncorrected intensities originally measured by UVIS/HDAC:

$$97 \quad I(r) = I_{corr}(r) + 4500 \quad [counts/s] \quad (2)$$

98 The observational geometry (spacecraft position and viewing direction of UVIS/HDAC) during the
99 swing by was also adopted from (Werner et al., 2004): On the Earth dayside CASSINI moved within
100 the ecliptic plane towards Earth. CASSINI's dayside trajectory as shown in (Werner et al., 2004 -
101 see Figure 1 there) is nearly linear within 3-15 R_e . It can be numerically approximated as radial
102 function of the GSE longitude:

$$103 \quad \phi_{GSE}(r) = 6.7 + 80.14/r \quad [^\circ] \quad (3)$$

104 with the geocentric distance r in R_e . Following (Werner et al., 2004) in this trajectory segment the
105 line of sight (LOS) of UVIS/HDAC pointed towards the positive GSE Y-axis away from Earth.

106 **3 Solar conditions and the interplanetary Lyman- α background**

107 On the swing by date 18 August 1999 the value of the total solar Lyman- α flux was $4.52 \cdot 10^{11}$
108 [photons/cm²/s]. It has been measured by TIMED SEE and SORCE SOLSTICE calibrated to UARS
109 SOLSTICE level [Woods et al., 2000] (provided by LASP, Laboratory For Atmospheric And Space
110 Physics, University of Boulder, Colorado). With the function given by (Emerich et. al., 2005), the
111 line-center solar Lyman- α flux was calculated from this total solar Lyman- α flux for the derivation
112 of the g -factor as used in Equation (4).

113 The solar activity level as indicated by the solar $F_{10,7cm}$ -radio flux starts to increase in summer 1999
114 from the low values of the solar minimum until 1998.

115 When flying at the Earth dayside between 3-15 R_e the UVIS/HDAC LOS pointed to a region with in-
116 terplanetary Lyman- α background of about 1400 R . This value was taken from the SOHO-SWAN all
117 sky map of the Lyman- α background of 17 August 1999 (SOHO-SWAN images provided via Web by
118 LATMOS-IPSL, Universit Versailles St-Quentin, CNRS, France: <http://swan.projet.latmos.ipsl.fr/images/>).

119 **4 Approach**

120 During the swing by at the Earth the UVIS/HDAC instrument measured Lyman- α radiation reso-
121 nantly backscattered from neutral hydrogen of the terrestrial exosphere and also from the interplan-
122 etary medium. Due to their low velocities the contributing H-atoms can be considered as "cold".



123 Therefore, this backscattered radiation contains wavelengths with a relatively narrow bandwidth
124 around the Lyman- α line center. The sole contribution of the interplanetary hydrogen was quantified
125 by the value taken from SOHO-SWAN as described in the previous section.

126 Within the exosphere the optical depth turns to be lower than 1 at geocentric distances $> 3 R_e$,
127 which allows for the assumption of single scattering. Under this assumption for a particular solar
128 Lyman- α radiation (manifested in the g-factor) the exospheric H-density $N(S)$ along a line of sight
129 S produces a Lyman- α scatter intensity I in [R]:

$$130 \quad I = \frac{g}{10^6} \int_0^{S_{max}} n(S)\epsilon(S)I_p(\alpha(S))dS \quad (4)$$

131 with $n(S)$ is the local H-density, $\epsilon(S)$ the local correction term for geocoronal selfabsorption/re-
132 emission and $I_p(\alpha(S))$ the local intensity correction for the angular dependence of the scattering.

133 Additionally to the solar radiation the dayside Lyman- α observations above $3R_e$ analysed in this
134 study are illuminated by a secondary Lyman- α radiation from lower atmospheric shells of the Earth:
135 At the dayside lower, optically thick exospheric shells are face-on illuminated by the Sun. The re-
136 emission created there acts as a secondary source of Lyman- α besides the Sun. The relative effect
137 increases with decreasing geocentric distance. With the $\epsilon(S)$ -term in Equation (4) the Lyman- α in-
138 tensity profile can be corrected from re-emission of solar Lyman- α from lower atmospheric shells of
139 the Earth. The applied method in this study, all considered correction terms and the used $\epsilon(r, \theta, \phi)$
140 map (shown in Figure 2) are in detail described in (Zoennchen et al., 2015).

141 With usage of a given H-density distribution the Lyman- α column brightness can be calculated for
142 any LOS and observing position within the optically thin regime based on the integral in Equation
143 (4). The calculated values ([R]) can be converted into their observable intensities ([counts/s]) using
144 a single instrumental factor ([counts/s/R]) - further referred as conversion factor f_c .

145 In this study two H-density models are used for comparison with UVIS/HDAC: the exospheric
146 $H(r, \theta, \phi)$ -density model derived from TWINS Lyman- α observations from 2008 and 2010 (Zoen-
147 nchen et al., 2015) and a radial symmetric model as introduced by (Chamberlain, 1963) and fre-
148 quently used for example by (Rairden et al., 1986), (Fuselier et al., 2010, 2020) or (Connor &
149 Carter, 2019):

$$150 \quad n_H(r) = n_0 \cdot \left(\frac{10 R_e}{r} \right)^3 \quad (5)$$

151 with the geocentric distance r in R_e . The H-density at $10 R_e$ subsolar point (n_0) is set at 40 cm^{-3} ,
152 which is within the reported range of Connor & Carter (2019) that derived n_0 from the XMM soft
153 X-ray emission.

154 The comparison of the calculated profiles with the UVIS/HDAC profile was made for two reasons:
155 First, to compare their radial dependency and second, to derive the conversion factor f_c of UVIS/HDAC
156 by cross-calibrating it against the calculated profile from the TWINS H-density model in the radial
157 range $3.0\text{-}5.5 R_e$ (overlapping range). Dayside Lyman- α observations with impact distances inside



158 this overlapping range are available by both - UVIS/HDAC and TWINS. This method for evalua-
159 tion of f_c assumes, that the TWINS H-density model from 2008, 2010 also matches the exospheric
160 H-density distribution on 18 August 1999 due to comparable space weather conditions. Both, the
161 used TWINS and UVIS/HDAC observations were measured during quiet geomagnetic conditions
162 (minimum Dst index ≈ -30 nT; provided by the website of the WDC for Geomagnetism, Kyoto) and
163 low solar activity (Solar 10,7 cm ≤ 130).

164 Nevertheless, it is known from other studies, that the terrestrial exosphere show H-density variations
165 of about 10-20% caused by geomagnetic storms (i.e. Bailey & Gruntman, 2013; Zoennchen et al.,
166 2017; Cucho-Padin & Waldrop, 2018). Therefore we expect an error of the conversion factor by this
167 variations up to 20%.

168 5 Comparison of the observed UVIS/HDAC profile with calculated profiles

169 The observed dayside Lyman- α profile (column intensity) by UVIS/HDAC (approximated in Equa-
170 tion (2)) was compared to the calculated Lyman- α profiles (column brightness) from two exospheric
171 H-density models described in the previous section. CASSINI's trajectory at the dayside between
172 3-15 R_e , the LOS of HDAC, the interplanetary background and the solar conditions of the swing by
173 day 18 August 1999 were considered by the calculation.

174 Figure (3A) shows the uncorrected observed Lyman- α profile by UVIS/HDAC from Equation (2)
175 in [counts/s] (black line) together with the calculated column brightness profiles in [R] based on the
176 TWINS 3D H-density model (red line) and the $1/R^3$ model (blue line) - all including interplanetary
177 Lyman- α background. It is obvious from that figure, that between 3-8 R_e the radial dependence of
178 the calculated profile using the TWINS 3D H-density model corresponds well to the UVIS/HDAC
179 observed profile. The radial dependency of the $1/R^3$ -profile (blue line) deviates from the HDAC
180 profile in this particular range.

181 Figure (3B) shows the ratios of the observed and the calculated profiles: In the overlapping range
182 (3.0-5.5 R_e) the averaged ratio between the UVIS/HDAC observations and the TWINS 3D H-density
183 model (red line) is nearly constant with only slight variations between -2.1% and +1.2%. It is equiv-
184 alent to the averaged conversion factor and was found to be $f_c=3.285$ [counts/s/R].

185 For the $1/R^3$ model (blue line) the ratio shows significant deviations from a constant value for lower
186 radial distances $<8R_e$. But for distances above 9 R_e the profile of this model turned also into a
187 nearly constant ratio to the UVIS/HDAC data (average = 3.145 [counts/s/R]).

188

189 Besides the cross-calibration method there is another independent way to approximate f_c : (Werner
190 et al, 2004) estimated the interplanetary Lyman- α background in the UVIS/HDAC observations with
191 4500 [counts/s]. To be not contaminated with exospheric emission, this value had to be measured
192 far enough outside the exosphere. The interplanetary Lyman- α radiation is also created by resonant



193 backscattering and is therefore comparable in its physical properties to exospheric emission. Using
194 the Lyman- α background emission value from SOHO-SWAN in [R] for the UVIS/HDAC LOS, the
195 conversion factor f_c can be approximated on this separate way to:

$$196 \quad f_c = \frac{4500 \text{ counts/s}}{1400 R} = 3.215 \text{ [counts/s/R]} \quad (6)$$

197 The two results for f_c with $f_c=3.285$ from the profile comparison using the TWINS H-density model
198 and $f_c=3.215$ from the background estimation by (Werner et al., 2004) are relatively close together.

199 **6 H-density profile derived from the UVIS/HDAC observations**

200 We applied the determined conversion factor $f_c=3.285$ [counts/s/R] to convert the observed dayside
201 Lyman- α profile by UVIS/HDAC from intensities [counts/s] into column brightness [R] between
202 3-15 R_e . Inverse usage of Equation (4) with known column brightnesses I(S) allows to fit the H-
203 density profile. The H-density profile inverted from the UVIS/HDAC observations was fitted into
204 the radial symmetric function:

$$205 \quad n_H(r) = 370520 * (r + 2.47)^{-3.67} \text{ [cm}^{-3}\text{]} \quad (7)$$

206 with geocentric distance r in R_e . Figure (4) shows the fitted H-density profile (black line). From the
207 $n_H(r)$ -profile the UVIS/HDAC observations can be calculated very precisely over the entire radial
208 range 3-15 R_e within $\pm 2\%$ error.

209 Obvious in Figure (4) is a change in the radial dependency of the profile in the radial region above
210 8 R_e . At distances lower 8 R_e the H-density profile seems to fall with distance with a power law \approx
211 $r^{-2.37}$ (red line in Figure (4)). It was fitted in the distance range 3-7 R_e to:

$$212 \quad n_H(r) = 10198 * r^{-2.375} \text{ [cm}^{-3}\text{]} \quad (8)$$

213 where the geocentric distance r is in R_e . The black and red lines are in very good agreement at
214 3-7 R_e . Above $>8 R_e$ the situation has changed and the H-density falls with about $\approx r^{-3}$, what is
215 indicated by the very good agreement of the cyan with the black line there. The fit of the H-density
216 profile between 9-15 R_e delivers a r^{-3} fall:

$$217 \quad n_H(r) = 35.17 * \left(\frac{10 R_e}{r} \right)^{3.02} \text{ [cm}^{-3}\text{]} \quad (9)$$

218 From theory an enhanced loss of neutral H atoms near the magnetopause and outside the magne-
219 tosphere can be expected due to sharply increased interactions with solar wind ions in this region
220 that produces soft X-ray photons and ENAs. The faster decrease with r^{-3} in the H-density profile
221 above 8 R_e might indicate the higher ionization of cold exospheric neutrals near the magnetopause
222 (located at 9-11 R_e in the vicinity of the sub solar point) and beyond.

223 From the fitted H-density profile of Equation (7) the exospheric H-density at 10 R_e was found to be
224 35 cm^{-3} at the ecliptic dayside. From known variations of the neutral exosphere due to geomagnetic



225 storms up to 20 % and with the summarized error from other contributions (i.e. from background,
226 solar Lyman- α flux and so on) there is a total error in the H-density of about 25 % expectable. Never-
227 theless, from several facts we assume, that the found value of 35 cm^{-3} at $10 R_e$ is more likely to be
228 a lower limit: First, between 3-10 R_e the neutral exospheric response to geomagnetic storms is so far
229 known as an increase and not as a decrease of neutral density (Bailey & Gruntman 2013, Zoennchen
230 et al., 2017, Cucho-Padin & Waldrop 2018). Second, there are results from other studies, that an
231 increasing solar activity also corresponds to an increase of neutral density in this radial range, either
232 weak (Fuselier et al., 2020) or somewhat stronger (Zoennchen et al., 2015). The H-density model
233 from TWINS used here based on observations in 2008 and 2010 near solar minimum during quiet
234 days without storms. Therefore it represents likely an exosphere with neutral densities close to their
235 lowest values.

236 7 Discussion

237 Ecliptic dayside Lyman- α observations of the terrestrial H-exosphere between 3-15 R_e by UVIS/HDAC
238 onboard CASSINI were compared to calculated Lyman- α brightnesses using two different H-density
239 models: First, the H-density model based on TWINS Lyman- α observations from 2008, 2010 and
240 second, the $1/R^3$ -model introduced by (Chamberlain et al., 1963). The calculations considered the
241 HDAC Lyman- α observations, CASSINI's trajectory and the HDAC LOS published by (Werner et
242 al., 2004).

243 As first result it was found, that the radial dependence of the HDAC observations and the calculated
244 profile from the TWINS model are very similar, in particular in the radial range 3-8 R_e . The Cham-
245 berlain model shows significant deviations from the observed profile in this lower range.

246 To be able to convert the HDAC observations from [counts/s] into physical units [R] the averaged
247 conversion factor $f_c=3.285$ [counts/s/R] was derived in the radial range 3.0-5.5 R_e (overlapping re-
248 gion) from the ratio between the HDAC observations and the calculated Lyman- α brightnesses from
249 the TWINS model. Dayside LOSs with impact distances in the overlapping region are available
250 from both instruments - HDAC and TWINS LAD. Additionally a second independent way was used
251 to quantify the conversion factor $f_c=3.215$ [counts/s/R] by calculating the ratio between the esti-
252 mated background value given by (Werner et al., 2004) and the corresponding value taken from the
253 SOHO/SWAN map. Both values found for f_c are very close together.

254 With usage of $f_c=3.285$ the HDAC observations are inverted into a radial symmetric H-density pro-
255 file of the ecliptic dayside between 3-15 R_e . The derived density profile determined a H-density
256 value of 35 cm^{-3} at $10 R_e$ in the vicinity of the sub-solar point. The error is expected with 25 %.
257 Nevertheless, from different mentioned reasons it is more likely, that this value is closer to the lower
258 limit.

259 Also found was a faster decrease of the H-density for distances above 8 R_e (r^{-3}) compared to the



260 lower region $3-7 R_e$ ($r^{-2.37}$). This is consistent with an enhanced depletion of neutral H in the far-
261 upsun direction beyond $8 R_e$ reported by (Carruthers et al, 1976) based on Lyman- α images from
262 the Moon by Apollo 16 and also with observations of Mariner 5 (Wallace et al., 1970).

263 The faster H-density decrease above $8 R_e$ in the up-sun direction as quantified in this study may
264 indicate an enhanced ionization rate near the magnetopause and beyond, respectively, due to sharply
265 increased interactions there of neutral H atoms with solar wind ions.

266 *Acknowledgements.* The authors gratefully thank the TWINS team (PI Dave McComas) for making this work
267 possible. Hyunju K. Connor gratefully acknowledges support from the NSF grants, AGS-1928883 and OIA-
268 1920965, and the NASA grants, 80NSSC18K1042, 80NSSC18K1043, 80NSSC19K0844, 80NSSC20K1670,
269 and 80MSFC20C0019. We acknowledge the support from the International Space Science Institute on the ISSI
270 team 492, titled "The Earth's Exosphere and its Response to Space Weather".



271 References

- 272 Bailey, J., & Gruntman, M. (2011). Experimental study of exospheric hydrogen atom distributions
273 by Lyman- α detectors on the TWINSmission. *Journal of Geophysical Research*, 116, A09302.
274 <https://doi.org/10.1029/2011JA016531>
- 275 Bailey, J., & Gruntman, M. (2013). Observations of exosphere variations during geomagnetic storms. *Geophys-*
276 *ical Research Letters*, 40, 1907-1911. <https://doi.org/10.1002/grl.50443>
- 277 Baliukin, I., Bertaux, J.-L., Quémenerais, E., Izmodenov, V., & Schmidt, W. (2019). SWAN/SOHO Lyman- α
278 mapping: The hydrogen geocorona extends well beyond the Moon. *Journal of Geophysical Research: Space*
279 *Physics*, 124, 861-885. <https://doi.org/10.1029/2018JA026136>
- 280 Bishop, J., Geocoronal structure: The effect of solar radiation pressure and. plasmasphere interaction, *J. Geo-*
281 *phys. Res.*, 90, 5235- 5245, 1985.
- 282 Branduardi-Raymont, G., Wang, C., Dai, L., Donovan, E., Li, L., Sembay, S., et al. (2018). SMILE Defini-
283 tion study report (red book). ESA/SCI(2018)1. Retrieved from [https://sci.esa.int/web/smile/-/61194-smile-](https://sci.esa.int/web/smile/-/61194-smile-definition-study-report-red-book)
284 [definition-study-report-red-book](https://sci.esa.int/web/smile/-/61194-smile-definition-study-report-red-book)
- 285 Carruthers, G. R., Page, T., and Meier, R. R. (1976): Apollo 16 Lyman alpha imagery of the hydrogen geo-
286 corona, *J. Geophys. Res.*, 81, 1664-1672 <https://doi.org/10.1029/JA081i010p01664>
- 287 Chamberlain, J. W.: Planetary coronae and atmospheric evaporation, *Planet Space Sci.*, 11, 901-960, 1963.
- 288 Connor, H. K. and Carter, J. A. (2019), Exospheric neutral hydrogen density at the 10 R_e subsolar point
289 deduced from XMM-Newton X-ray observations, *Journal of Geophysical Research: Space Physics*,
290 [doi:10.1029/2018JA026187](https://doi.org/10.1029/2018JA026187).
- 291 Connor, H. K., Sibeck, D. G., Collier, M. R., Baliukin, I. I., Branduardi-Raymont, G., Brandt, P. C., et al. (2021).
292 Soft X-ray and ENA imaging of the Earth's dayside magnetosphere. *Journal of Geophysical Research: Space*
293 *Physics*, 126, e2020JA028816. <https://doi.org/10.1029/2020JA028816>
- 294 Cucho-Padin, G., & Waldrop, L. (2019). Time-dependent Response of the Terrestrial Exosphere to a Geomag-
295 netic Storm. *Geophysical Research Letters*, 46. <https://doi.org/10.1029/2019GL084327>
- 296 Domingo, V., Fleck, B., & Poland, A. I. (1995). SOHO: The solar and heliospheric observatory. *Space Science*
297 *Reviews*, 72, 81. <https://doi.org/10.1007/BF00768758>
- 298 Emerich, C., Lemaire, P., Vial, J.-C., Curdt, W., Schühle, U., Wilhelm, K. (2005): A new relation between the
299 central spectral solar HI Lyman- α irradiance and the line irradiance measured by SUMER/SOHO during the
300 cycle 23, *Icarus*, 178, 429-433. <https://doi.org/10.1016/j.icarus.2005.05.002>
- 301 Fahr, H. J., Nass, U., Dutta-Roy R. & Zoenchen, J. H. (2018): Neutralized solar wind ahead of the
302 Earth's magnetopause as contribution to non-thermal exospheric hydrogen. *Ann. Geophys.*, 36(2), 445-457.
303 <https://doi.org/10.5194/angeo-36-445-2018>
- 304 Fuselier, S. A., Funsten, H. O., Heirtzler, D., Janzen, P., Kucharek, H., McComas, D. J., et al. (2010). Ener-
305 getic neutral atoms from the Earth's sub-solar magnetopause. *Geophysical Research Letters*, 37, L13101.
306 <https://doi.org/10.1029/2010GL044140>
- 307 Fuselier, S. A., Dayeh, M. A., Galli, A., Funsten, H. O., Schwadron, N. A., Petrinec, S. M., et al. (2020). Neu-
308 tral atom imaging of the solar wind-magnetosphere-exosphere interaction near the subsolar magnetopause.
309 *Geophysical Research Letters*, e2020GL089362. 47. <https://doi.org/10.1029/2020GL089362>
- 310 Goldstein, J., & McComas, D. J. (2018). The big picture: Imaging of the global geospace environment by the



- 311 TWINS mission. *Reviews of Geophysics*, 56, 251-277. <https://doi.org/10.1002/2017RG000583>
- 312 Hodges Jr., R. R. (1994), Monte Carlo simulation of the terrestrial hydrogen exosphere, *J. Geophys. Res.*, 99,
313 23229-23247.
- 314 Jansen, F., Lumb, D., Altieri, B., Clavel, J., Ehle, M., Erd, C., et al. (2001). XMM-Newton observatory: I.
315 The spacecraft and operations. *Astronomy and Astrophysics*, 365(1), L1-L6. [https://doi.org/10.1051/0004-](https://doi.org/10.1051/0004-6361:20000036)
316 6361:20000036
- 317 Kusnierkiewicz, D. Y., "A description of the TIMED spacecraft," American Institute of Physics (AIP) Confer-
318 ence Proceedings, 387, Part One, pp. 115-121, 1997
- 319 McComas, D. J., Allegrini, F., Bochler, P., Bzowski, M., Christian, E. R., Crew, G. B., et al. (2009). Global
320 observations of the interstellar interaction from the Interstellar Boundary Explorer (IBEX). *Science*, 326,
321 959-962. <https://doi.org/10.1126/science.1180906>
- 322 Qin, J., and L. Waldrop (2016), Non-thermal hydrogen atoms in the terrestrial upper thermosphere, *Nat. Com-*
323 *mun.*, 7, 13655, doi:10.1038/ncomms13655.
- 324 Qin, J., Waldrop, L., & Makela, J. J. (2017). Redistribution of H atoms in the upper atmosphere
325 during geomagnetic storms. *Journal of Geophysical Research: Space Physics*, 122, 10686-10693.
326 <https://doi.org/10.1002/2017JA024489>
- 327 Sibeck, D. G., Allen, R., Aryan, H., Bodewits, D., Brandt, P., Branduardi-Raymont, G., et al. (2018). Imaging
328 plasma density structures in the soft X-rays generated by solar wind charge exchange with neutrals. *Space*
329 *Science Reviews*, 214(4), 124. article id. 79.
- 330 Waldrop, L., and L. J. Paxton (2013), Lyman- α airglow emission: Implications for atomic hy-
331 drogen geocorona variability with solar cycle, *J. Geophys. Res. Space Physics*, 118, 5874-5890.
332 <https://doi.org/10.1002/jgra.50496>
- 333 Wallace, L., Barth, C. A., Pearce, J. B., Kelly, K. K., Anderson, D. E., and Fastie, W. G. (1970):
334 Mariner 5 measurement of the Earth's Lyman alpha emission, *J. Geophys. Res.*, 75(19), 3769-3777.
335 <https://doi.org/10.1029/JA075i019p03769>.
- 336 Werner S., Keller H.U., Korth A., Lauche H. (2004): UVIS/HDAC Lyman- α observations of the geocorona
337 during Cassinis Earth swingby compared to model predictions, *Advances in Space Research*, Volume 34,
338 Issue 8, 2004, Pages 1647-1649, ISSN 0273-1177. <https://doi.org/10.1016/j.asr.2003.03.074>
- 339 Woods, T. N., Tobiska, W. K., Rottman, G. J., and Worden, J. R. (2000): Improved solar Lyman alpha irradi-
340 ance modeling from 1947 through 1999 based on UARS observations, *J. Geophys. Res.*, 105, 27195-27215.
341 <https://doi.org/10.1029/2000JA000051>
- 342 Zoennchen, J. H., Bailey, J. J., Nass, U., Gruntman, M., Fahr, H. J., & Goldstein, J. (2011). The TWINS
343 exospheric neutral H-density distribution under solar minimum conditions. *Annales de Geophysique*, 29(12),
344 2211-2217. <https://doi.org/10.5194/angeo-29-2211-2011>
- 345 Zoennchen, J. H., Nass, U., and Fahr, H. J. (2013): Exospheric hydrogen density distributions for equinox
346 and summer solstice observed with TWINS1/2 during solar minimum, *Ann. Geophys.*, 31, 513-527.
347 <https://doi.org/10.5194/angeo-31-513-2013>
- 348 Zoennchen, J. H., Nass, U., and Fahr, H. J. (2015): Terrestrial exospheric hydrogen density distributions under
349 solar minimum and solar maximum conditions observed by the TWINS stereo mission, *Ann. Geophys.*, 33,
350 413-426. <https://doi.org/10.5194/angeo-33-413-2015>



- 351 Zoennchen, J. H., Nass, U., Fahr, H. J., & Goldstein, J. (2017): The response of the H geocorona between 3
352 and 8 R_e to geomagnetic disturbances studied using TWINS stereo Lyman- α data. Ann. Geophys., 35(1),
353 171-179. <https://doi.org/10.5194/angeo-35-171-2017>



Figure Captions

Fig. 1. Black: UVIS/HDAC Lyman- α intensity profile [counts/s] (black line) from (Werner et al., 2004); the origin of the two peaks were identified by (Werner et al., 2004) as (A) the Earthmoon and (B) distortion by the radiation belt; Red: numerical approximation of the intensity profile from Equation (1).

Fig. 2. Local ratio $\epsilon(r, \theta, \phi)$ of the local Lyman- α illumination (influenced by multiple scattering effects) and the original solar illumination within the ecliptic plane calculated with a multiple scattering Monte Carlo model (Zoennchen et al., 2015).

Fig. 3. (A) observed, uncorrected Lyman- α profile by UVIS/HDAC in [counts/s] from Equation (2) (black line) and the calculated column brightness profiles based on the TWINS 3D H-density model (red line) and the $1/R^3$ model (blue line), both including background and in [R]
(B) ratios between the UVIS/HDAC observed and the calculated profiles: with the TWINS H-density model (red line) and with the $1/R^3$ model (blue line).

Fig. 4. (Black line): Radial symmetric H-density profile (Equation (7)) fitted from UVIS/HDAC observations; (Red line): Powerlaw fit of the H-density profile in the lower radial range 3-7 R_e ; (Cyan line): Powerlaw fit of the H-density profile in the upper radial range 9-15 R_e ; The deviation of the red and the cyan lines from the black line indicate, that the H-density profiles falls faster at larger distances $>8 R_e$ than at lower distances $<8 R_e$.



Figures:

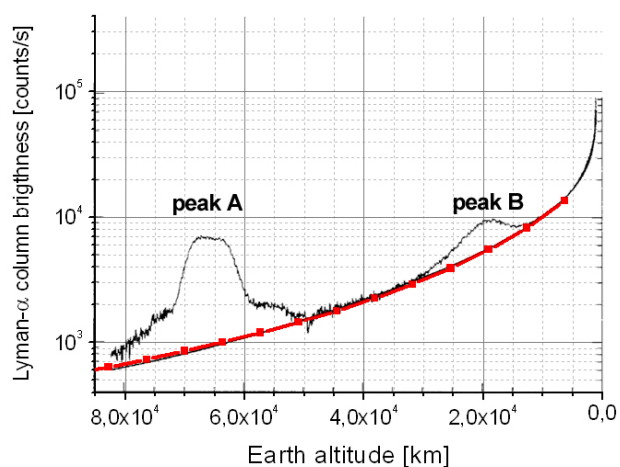


Fig. 1. Black: UVIS/HDAC Lyman- α intensity profile [counts/s] (black line) from (Werner et al., 2004); the origin of the two peaks were identified by (Werner et al., 2004) as (A) the Earthmoon and (B) distortion by the radiation belt; Red: numerical approximation of the intensity profile from Equation (1)

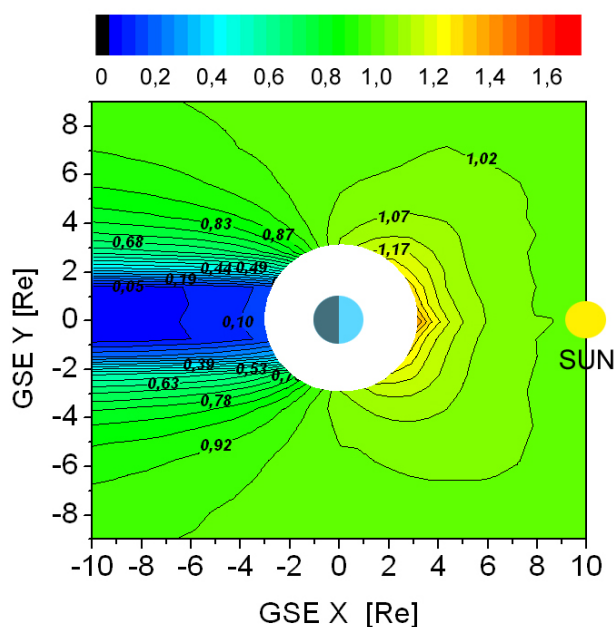


Fig. 2. Local ratio $\varepsilon(r,\theta,\phi)$ of the local Lyman- α illumination (influenced by multiple scattering effects) and the original solar illumination within the ecliptic plane calculated with a multiple scattering Monte Carlo model (Zoennchen et al., 2015)

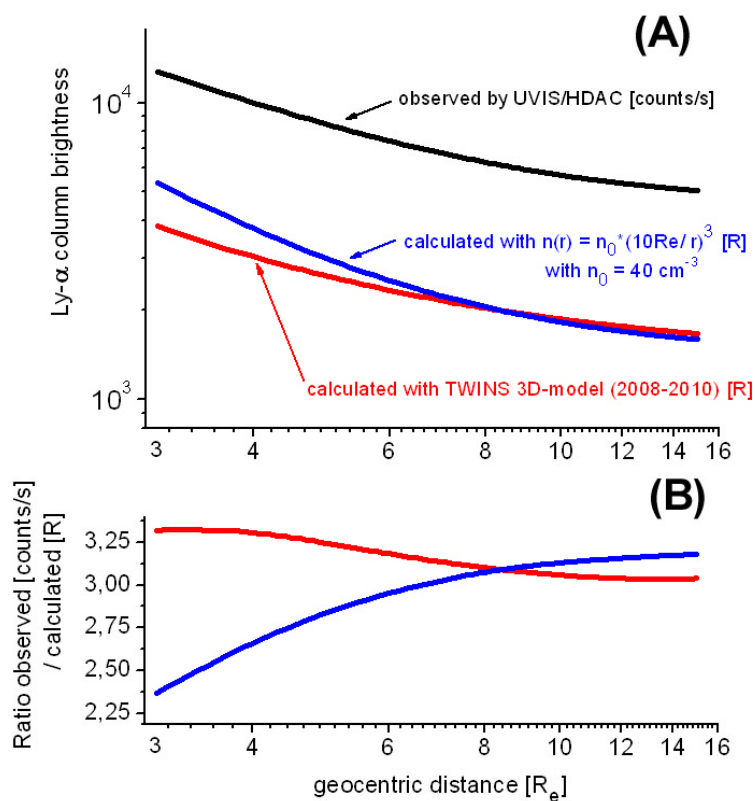


Fig. 3. (A) observed, uncorrected Lyman- α profile by UVIS/HDAC in [counts/s] from Equation (2) (black line) and the calculated column brightness profiles based on the TWINS 3D H-density model (red line) and the $1/R^3$ model (blue line), both including background and in [R]
(B) ratios between the UVIS/HDAC observed and the calculated profiles: with the TWINS H-density model (red line) and with the $1/R^3$ model (blue line).

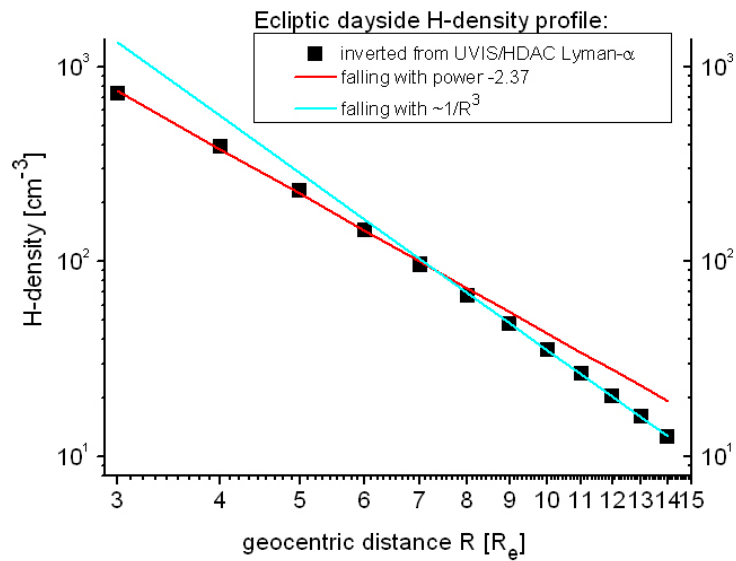


Fig. 4. (Black line): Radial symmetric H-density profile (Equation (7)) fitted from UVIS/HDAC observations; (Red line): Powerlaw fit of the H-density profile in the lower radial range 3-7 R_e ; (Cyan line): Powerlaw fit of the H-density profile in the upper radial range 9-15 R_e ; The deviation of the red and the cyan lines from the black line indicate, that the H-density profiles falls faster at larger distances $>8 R_e$ than at lower distances $<8 R_e$.